Research Article Vol. 10, No. 10 / October 2023 / Optica 1253

2.2 kW single-mode narrow-linewidth laser delivery through a hollow-core fiber

M. A. Cooper,[1] J. Wahlen,[1] S. Yerolatsitis,[1] D. Cruz-Delgado,[1] D. Parra,[1] B. Tanner,[2] P. Ahmadi,[3] O. Jones,[2] Md. S. Habib,[4] I. Divliansky,[1] J. E. Antonio-Lopez,[1] A. Schülzgen,[1] and R. Amezcua Correa[1,*]

[1]CREOL, The College of Optics and Photonics, University of Central Florida, 4304 Scorpius St, Orlando, Florida 32816, USA
[2]Coherent Corp, 3340 Parkland Ct, Traverse City, Michigan 49686, USA
[3]Coherent Corp, 1280 Blue Hills Avenue, Bloomfield, Connecticut 06002, USA
[4]Florida Institute of Technology, Department of Electrical Engineering and Computer Science, 150 W University Blvd, Melbourne, Florida 32901, USA
*r.amezcua@creol.ucf.edu

Received 25 May 2023; revised 30 August 2023; accepted 30 August 2023; published 22 September 2023

Antiresonant hollow-core fibers (AR-HCFs) have opened up exciting possibilities for high-energy and high-power laser delivery because of their exceptionally low nonlinearities and high damage thresholds. While these fiber designs offer great potential for handling kilowatt-class powers, it is crucial to investigate their performance at multi-kW power levels. Until now, transmission of narrow-linewidth single-mode lasers at multi-kW power levels through a HCF has not been demonstrated, to our knowledge. Here, we present the delivery of a record 2.2 kW laser power with an input spectral linewidth of 86 GHz, centered at 1080 nm, while maintaining 95% transmission efficiency and beam quality (M^2) of 1.03. This was achieved via a 104.5 m single-mode five-tube nested AR-HCF with 0.79 dB/km loss. Furthermore, we show power delivery of 1.7 kW with a spectral linewidth as narrow as 38 GHz through the same fiber. Our results could lead to a new generation of fiber-based laser beam delivery systems with applications in precision machining, nonlinear science, directed energy, and power beaming over fiber.

https://doi.org/10.1364/OPTICA.495806

1. INTRODUCTION

In recent years, the delivery of high-power single-mode laser beams through hollow-core optical fibers has undergone substantial experimental advancements. These developments have been driven by the potential application of this technology in key areas such as precision manufacturing [1], ultrafast physics [2–5], telecommunications [6–9], directed energy [10,11], and power-beaming over fiber [12], to mention a few. In general, the goal of single-mode laser beam delivery fiber is to preserve the spectral and spatial features of the source at a remote point of interest. This is especially relevant in applications where beam focusing near the diffraction limit is required to achieve high precision and accuracy. Nevertheless, high-power transmission through solid core fibers at long lengths suffers from numerous deleterious phenomena due to intensity-based nonlinear effects such as the Kerr effect, stimulated Raman scattering (SRS), and stimulated Brillouin scattering (SBS) [13–15]. These effects impose significant constraints on single-mode narrow-linewidth power levels that can be transmitted through a solid-core optical fiber. In particular, high-power single-mode narrow-linewidth ytterbium-doped fiber laser amplifiers (YDFAs) are typically restricted by SBS, while SRS limits high-power broadband performance [16].

Thus far, most kilowatt-class laser delivery studies through solid core fibers over distances of at least a few tens of meters have been performed with broadband sources. For example, low-numerical-aperture multimode step index fibers have enabled transmission of 5 kW over 20 m [17], 800 W over 100 m [18], and 1 kW over 100 m [19] with output beam quality (M^2) ~1.3. Additionally, by utilizing few-mode photonic crystal fibers designed to encourage large higher-order mode losses, 1 kW over 300 m with an output $M^2 = 1.7$ [20] and 10 kW over 30 m [21] have been demonstrated. Despite these achievements, these fibers are not ideal for flexible beam delivery systems in applications demanding strict preservation of the spatial and spectral properties of the source due to their high sensitivity to bending and nonlinear effects present in the silica core. Moreover, single-mode multi-kW laser power transmission at linewidths of less than 100 GHz has not been reported over fiber lengths close to 100 m, to the best of our knowledge. To surpass the capabilities of silica core fiber technologies in laser delivery, it is crucial to investigate novel guidance mechanisms for suppressing nonlinear effects and promoting robust single-mode propagation.

The concept of a photonic bandgap introduced the possibility of guiding light within an air core confined by a precisely engineered silica glass–air cladding structure [22]. Since then, hollow-core fibers (HCFs) have been extensively investigated,

leading to tremendous performance improvements and the demonstration of attenuation levels comparable to standard single-mode fibers [6,9,23–31]. In this regard, the emergence of antiresonant HCFs (AR-HCFs) offered unprecedented versatility in terms of tailoring fiber modal properties and great promise for ultra-low-loss light guidance [8,9,29–34]. In general, these structures consist of a negative curvature air–core interface, and rely on AR and inhibited coupling as the light guiding mechanism [31,35,36]. Various AR-HCF structures have been demonstrated, ranging from single resonator rings [25] and conjoined tubes [29] to nested [32] and double nested [8] configurations, ranging from strictly single-mode to multimode designs [26].

A unique feature of HCF is that light can be guided with a minimal fraction of the field overlapping with the glass structure, increasing the damage threshold and reducing material absorption and nonlinearity. Over the years, there have been numerous efforts on power transmission through HCFs, including photonic bandgap [37] and hypocycloidal Kagome-type designs [38] with single-mode laser power transmission experiments reaching up to 1.2 kW through 1.5 m of fiber [39]. Recent AR-HCF structures have shown great promise for scaling to extreme high-power single-mode delivery, due to their strong confinement, and large core diameter characteristics. As such, interest in exploring high-power delivery through AR-HCFs has greatly intensified since the demonstration of 300 W single-mode broadband laser transport at 1 μm through a seven-tube AR-HCF [40]. At the ∼1000 W level, there have been transmission demonstrations involving broad-linewidth sources through both nested and non-nested AR-HCF designs [34,41,42]. Significantly, a recent study by Mulvad *et al*. [34] successfully delivered 1.1 kW output power over 1 km of nested AR nodeless fiber (NANF) using a 1080 nm source with a spectral linewidth of approximately 5 nm. However, despite these significant advancements, the transmission of multi-kW powers or high-power narrow-linewidth sources in a single-mode fashion needs to be investigated. Additionally, these studies have highlighted the challenge of maintaining adequate coupling efficiency and preventing failure at the fiber input, requiring optical alignment adjustments during high-power operation.

In this work, we demonstrate transmission of multi-kW narrow-linewidth single-mode power over 104.5 m and 6.25 m of five-tube NANF. In the case of the 104.5 m fiber, by coupling a 2.3 kW single-mode continuous wave (CW) laser operating at 1080 nm and 86 GHz linewidth, we achieved an output power of 2.198 kW, while maintaining near-diffraction-limited beam quality $M^2 = 1.03$. Moreover, for laser configurations with linewidths of 63 GHz and 38 GHz, we obtained output powers of 2.18 kW and 1.7 kW, respectively, limited only by the maximum power of the source. Interestingly, we observed no nonlinear SRS and SBS effects from glass. However, at high powers, additional discrete frequency peaks appear in the output spectrum, due to rotational SRS from atmospheric nitrogen in the fiber's core.

2. EXPERIMENTAL DESIGN

The low-loss NANF used in the experiments was manufactured in-house using the stack-and-draw method with an attenuation of 0.79 dB/km at 1080 nm. We selected a five-tube nested design for the robust single-mode operation expected by this structure due to its large higher-order mode loss and its low fundamental mode loss [43]. The fiber is coated with a single 40 μm thick layer of high-index polymer. In Fig. 1(a), we present a scanning electron microscope (SEM) image of the uncoated fiber facet showing a core diameter of ∼23 μm and thickness of outer tubes and nested tubes of 780 nm ± 10 nm.

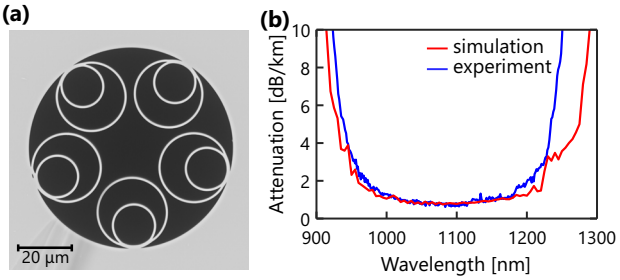

Fig. 1. Characterization of the fabricated fiber. (a) SEM image of the five-nested-tube NANF. (b) Simulated (red) and measured (blue) spectral attenuation.

In Fig. 1(b) we present the measured attenuation spectrum obtained via a cutback method. To do so, the transmission spectrum was measured by coupling a white light source (NKT SuperK COMPACT) into a 463 m long fiber on a 30 cm diameter coil. Then, while maintaining constant input conditions, the fiber was cut back to 100 m. The transmission was measured again, and by comparing the two, we obtained the spectral attenuation. A cutback to 100 m fiber length allowed us to accurately obtain the losses of the fundamental mode. The attenuation including surface scattering, confinement, and bend losses at 30 cm coil diameter, was simulated considering the fiber parameters described above using a finite element method mode solver (COMSOL Multiphysics) [43]. The calculated bend loss is 0.11 dB/km for 30 cm bend diameter and remains below 1 dB/km for diameters greater than 12 cm. Additionally, the calculated loss of the first higher-order mode group (LP_{11}) is ∼9.5 dB/m at 1080 nm. The mode field diameter (MFD) of the fundamental mode was measured using a 10× magnification 4-f imaging telescope at the fiber output and compared to a commercially available fiber (Coherent LMA-GDF-20/400) with a known 17.1 μm MFD as reference. Considering the $1/e^2$ definition [44], the MFD was found to be ∼18 μm at 1080 nm, which is in excellent agreement with the simulated MFD.

To investigate the power delivery performance of the NANF, we employed an unpolarized CW fiber laser amplifier system capable of producing up to 2315 W at a 86 GHz linewidth and an M^2 of 1.06 ± 0.02. The laser source utilized a three-stage YDFA architecture and an external seed laser modulated by an acousto-optic modulator driven by an RF white noise source for spectral broadening [45]. The seed operated at a wavelength of 1080 nm at a linewidth of 1 MHz. Inline RF attenuators on the input of the phase modulator served as a mechanism for controlling the linewidth of the laser beam.

Figure 2(a) shows a schematic of the high-power transmission setup. The laser's large mode area (LMA) fiber output beam was collimated using a plano–convex lens (L_1). The resulting collimated beam was then free space coupled to the five-tube NANF. Although no active pointing stabilization methods were employed in this work, the optical path length between the laser LMA fiber output and the HCF input was 20 cm to minimize pointing jitter. A second plano–convex lens (L_2) is selected to precisely match the MDF of the NANF, resulting in a numerically calculated maximum coupling efficiency of ∼98% into the fundamental mode. Low-OH fused silica lenses L_1, L_2, L_3, and a standard-grade fused-silica lens L_4 are anti-reflection coated providing less than 0.1%

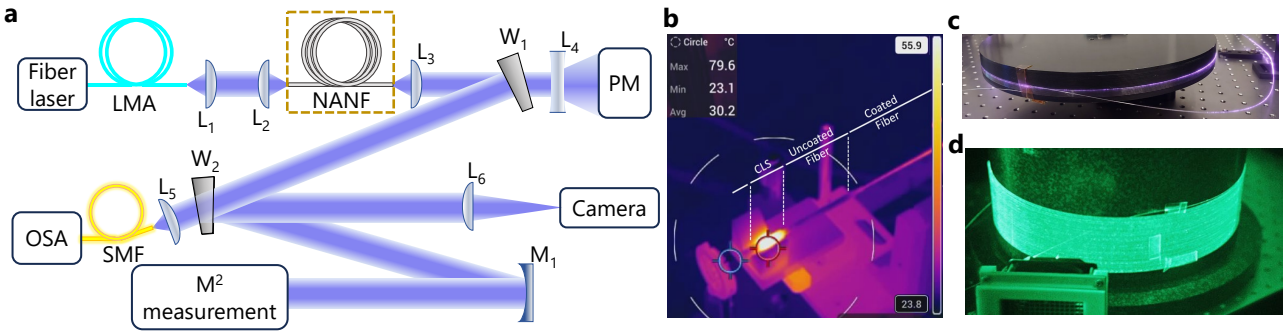

Fig. 2. (a) Schematic of high-power transmission setup. A high-power CW fiber laser is coupled into a NANF. LMA, large mode area fiber; SMF, single-mode fiber; L_1, L_2, L_3, L_5, L_6, plano–convex lenses; L_4, bi-concave lens; W_1, W_2 fused silica wedges; PM, power meter; OSA, optical spectrum analyzer; M_1, plano–concave mirror. (b) Thermal image of fiber input and cladding light stripper for 2.3 kW input power. (c) Aluminum mandrel used for fiber management in 6.25 m transmission test. (d) Near infrared image of the polystyrene drum used for fiber coiling during 104.5 m test.

reflection. To help minimize localized thermal drift and damage during high-power operation, a 1 cm long cladding light stripper (CLS) was applied through chemical etching [46] behind the input facet of the fiber. The fiber was mounted on a quartz block fixture using high-temperature epoxy. In our experiment, only about 5 cm of fiber was uncoated at the input and output ends, as depicted in Fig. 2(b). Precise alignment between the laser source output LMA and the NANF input facet was achieved using two five-axis stages.

We conducted power delivery experiments on two distinct fiber sections, measuring 6.25 m and 104.5 m in length. By initially conducting power delivery experiments on the short 6.25 m fiber, we were able to optimize fiber preparation and configure the experimental layout without the risk of accidentally damaging a significant portion of the NANF. Once power transmission was characterized using the 6.25 m fiber, further investigation was conducted with the 104.5 m fiber. The 6.25 m NANF was wrapped around an uncooled 30 cm diameter grooved aluminum mandrel, as shown in Fig. 2(c). The grooved design of the mandrel served the dual purpose of preventing fiber overlap and aiding in temperature monitoring during testing. The longer 104.5 m fiber was wrapped on a 30 cm diameter polystyrene drum, as depicted in Fig. 2(d). The NANF output was collimated using the same mounting method as at the input and directed through W_1. The low-power reflection from the front surface of the wedge was fed into the beam diagnostic equipment. Over 99.8% of the fiber output power was captured and measured using a 5 kW power meter (Ophir 5000 W-BB-50).

We characterized the output beam through M^2, spectral and mode profile measurements. To accomplish this, we utilized the first reflection of W_1 as a low-power pickoff, which was directed towards W_2. The light transmitted through W_2 was then coupled via L_5 to an optical spectrum analyzer (OSA) with a resolution of 7.5 GHz (Thorlabs OSA202C) using a single-mode fiber patch cable. Simultaneously, the front surface reflection of W_2 was reflected off a concave mirror (M_1) and directed towards a beam profiler (Thorlabs BP209-IR2) to measure the beam divergence and M^2 in the x and y directions. We determined M^2 using the ISO/TR 11146-3:2004 standard. For beam imaging, the reflection from the back surface of W_2 was captured by a CMOS camera through a 400 mm focal length lens (L_6). During the 6.25 m test, we used a DataRay WinCamD camera, while the 104.5 m test employed a Gentec Beamage 3.0 camera. It is important to note that in our experimental setup, the imaged beam originates from back surface reflection of W_2, resulting in the beam passing through the wedge material twice. This leads to a very slight elliptical distortion at the image plane due to a phase difference across the beam caused by its propagation through the wedge material.

3. POWER DELIVERY RESULTS AND DISCUSSION

The first evaluation at high power was conducted with an 86 GHz linewidth on the 6.25 m NANF and was subsequently repeated for each linewidth at 63 GHz and 38 GHz. Following this, we extended our testing to the 104.5 m fiber at the three investigated linewidths. Coupling from the laser LMA fiber to the NANF was performed at low power (below 5 W). At this stage, we measured a transmission efficiency ($TE = P_{out}/P_{in}$) of 97.3% and 96.2% for the 6.25 m and 104.5 m fibers, respectively. Here, P_{out} is the output power, and P_{in} is the power launched into the fiber. P_{in} was measured by removing L_2, the NANF, and L_3 from the experimental setup. Therefore, TE accounts for coupling and propagation losses. The approximately 1.1% difference in TE between the 6.25 m and 104.5 m fibers highlights the low fiber loss. After optimizing coupling at low power, we increased the power to ∼20 W. This higher power allowed us to verify alignment of the optical diagnostic components, as illustrated in Fig. 2(a). After aligning the diagnostics, we gradually increased the power in increments of ∼220 W. At each input power, we allocated a 120 s pause to monitor any potential thermal drift and to ensure that the power meter reached a steady state before recording the measurements. The fiber temperature was continuously monitored using a handheld thermal camera (FLIR T560). Throughout the study, the temperature on the CLS remained below 82°C. Additionally, the temperature along the initial tens of centimeters of fiber did not exceed 42°C on the 6.25 m or 49°C on the 104.5 m transmission test, well below the thermal limit of the fiber coating of ∼100°C. The highest recorded temperature was due to scattered light at the input CLS, as shown in Fig. 2(b).

Figures 3(a)–3(c) present the high-power delivery results for the three different spectral linewidth conditions through the 6.25 m and 104.5 m lengths in black and red, respectively. The maximum power of the source was dependent on the linewidth: 2.315 kW at 86 GHz and 63 GHz, and SBS limited to 1.828 kW at 38 GHz. When operating at 38 GHz, the laser system automatically shuts down above 1.828 kW to prevent damage due to backscattered light. The power delivered through the 6.25 m NANF versus input power is presented in Figs. 3(a)–3(c) in black. In this case, maximum output powers of 2.205 kW, 2.172 kW, and 1.708 kW

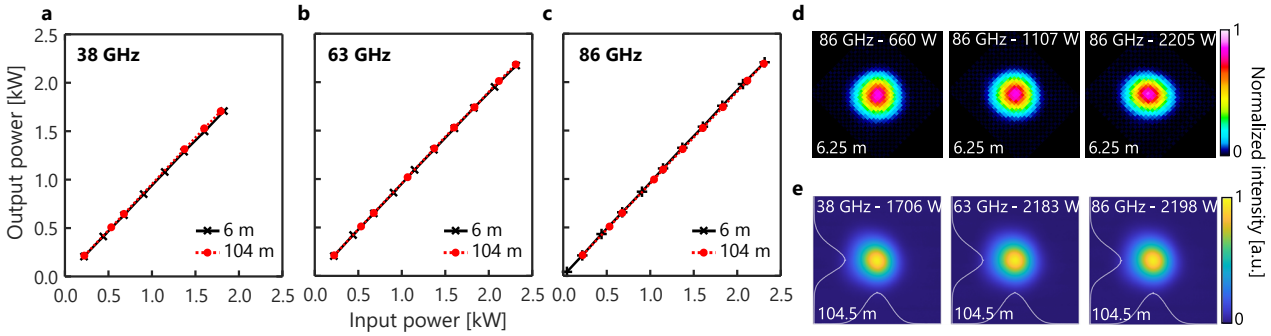

Fig. 3. Output power as function of input power at a source linewidth of (a) 38 GHz, (b) 63 GHz, and (c) 86 GHz for a fiber length of 6.25 m (black) and 104.5 m (red). (d) Near field beam profiles at the 6.25 m NANF output for different transmitted powers for 86 GHz linewidth. (e) Near field beam profiles on the output of the 104.5 m NANF at maximum transmitted power at 38 GHz, 63 GHz, and 86 GHz linewidth.

Table 1. Summary of Beam Quality and Transmission Efficiency Measurements at Highest Power Tested at Each Input Linewidth through Hollow-Core Fiber Lengths of 6.25 m and 104.5 m

Test			Output		
P_{in} (W) ±4%	Linewidth ±3%	Length ±10 cm	P_{out} (W) ±4%	M^2 ±5%	TE ±1%
2315	86 GHz	6.25 m	2205	1.020	95.2%
2310	86 GHz	104.5 m	2198	1.032	95.1%
2315	63 GHz	6.25 m	2172	1.025	93.8%
2310	63 GHz	104.5 m	2183	1.035	94.5%
1828	38 GHz	6.25 m	1708	1.039	93.4%
1791	38 GHz	104.5 m	1706	1.022	95.3%

were achieved at 86 GHz, 63 GHz, and 38 GHz, respectively. These values correspond to TE of 95.2%, 93.8%, and 93.4% for each respective linewidth. The slightly lower efficiencies observed for the latter two cases can be attributed to micrometer-scale misalignment of the input coupling conditions. It is important to note that the fiber launching conditions were not re-optimized during the experiments to minimize risk of fiber damage during high-power operation. Similarly, the power delivered through the 104.5 m fiber reached 2.198 kW, 2.183 kW, and 1.706 kW at 86 GHz, 63 GHz, and 38 GHz, respectively. Correspondingly, the transmission efficiencies for these source linewidths were 95.1%, 94.5%, and 95.3%. Near field beam profiles from the 6.25 m fiber output, captured at power levels of 0.6 kW, 1 kW, and 2.2 kW at 86 GHz are presented in Fig. 3(d). Likewise, output beam profiles from the 104.5 m fiber at maximum delivered powers are shown in Fig. 3(e). Furthermore, beam quality measurements were conducted throughout testing, indicating near-diffraction-limited beam quality. In Table 1, we present a summary of the high-power delivery measurements, including the associated transmission efficiency and beam quality. The M^2 value is reported as $M^2 = \sqrt{M_x^2 \cdot M_y^2}$.

We conducted spectral measurements for different power levels and source linewidths. Figures 4(a)–4(c) show the spectrum of the high-power source for the three linewidths in blue. These figures also display the spectra after propagation through the 104.5 m fiber for an output power of 1.5 kW and at the maximum output power. It is important to note that the spectra obtained for the 6.25 m NANF are not shown in Fig. 4, as no spectral distortions were observed during high-power testing for this length. Notably, in the insets in Figs. 4(a)–4(c), we can observe that the NANF output spectra maintain an almost unperturbed central peak of the source at 1080 nm. Hence, the full width-half-maximum and spectral shape of the source are well preserved after propagation. However, for $P_{out} = 1500$ W, a series of discrete peaks centered around 1090 nm becomes visible in the output spectra. With increasing power, at $P_{out} = 2.2$ kW, additional peaks developed around 1100 nm. In our experiments, we did not observe any additional peaks outside the plotted wavelength range, nor did we observe them for output powers below 1.4 kW.

Based on the rotational and vibrational Raman responses of atmospheric air [47], the spectral peaks can be attributed to the Raman response of nitrogen within the NANF core, predominantly due to rotational SRS on the S-branch [48,49] The measured output spectra for $P_{out} = 2.2$ kW clearly exhibit both the first-order Stoke shift and second-order Stokes shift, as depicted in Figs. 4(b) and 4(c). Within these spectra, we can identify five distinct rotational lines within the first Stokes shift near 1090 nm, three rotational states in the second Stokes shift near 1100 nm, and a very weak anti-Stokes line near 1070 nm. The primary nonlinear mechanism contributing to the observed spectral peak generation arises from rotational SRS within the atmospheric nitrogen present in the core, rather than nonlinearities within the glass structure. This can be attributed to the minimal spatial overlap between the fundamental mode and silica, which is approximately $\sim 1.2 \times 10^{-4}$ for our fiber. It is worth noting that rotational SRS due to atmospheric nitrogen within a NANF was recently reported in high-power transmission experiments, when transmitting 1.1 kW CW broadband laser power through a 1 km fiber [34].

However, our results represent the first observation of discrete CW SRS laser line generation at kW powers in a HCF, to the best of our knowledge. Considering power delivery applications, this nonlinearity can be effectively mitigated by applying vacuum within the core or by purging it with a non-Raman active gas such as argon. From a different perspective, this effect could be exploited to create novel AR-HCF-based laser sources capable of generating high CW powers at wavelengths that are challenging to access using rare-earth-doped solid-core fibers. This could be achieved by filling the NANF core with a tailored gas composition and pressure in combination with pumping with a suitable narrow-linewidth source.

To calculate the maximum NANF length to deliver the 2.3 kW source while avoiding the onset of rotational nitrogen SRS, we consider a power threshold for SRS onset ($P_{th(SRS)} = 1400$ W).

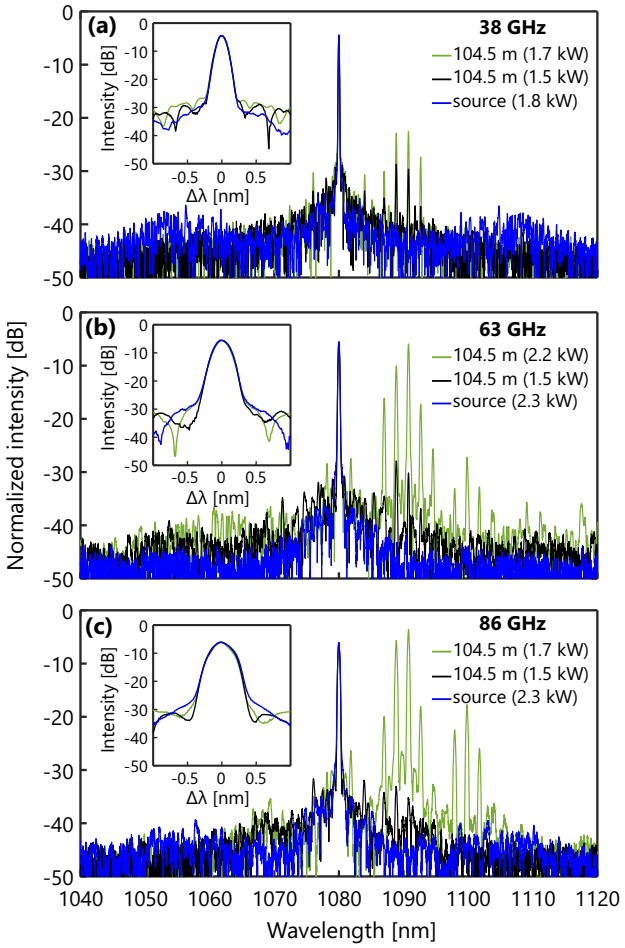

Fig. 4. Spectral characterization of the laser source versus NANF output. Spectral measurements obtained for source linewidth configurations at (a) 38 GHz, (b) 63 GHz, and (c) 86 GHz. Measured input signal spectra from the laser source (blue) are compared to a 1.5 kW NANF output (black) and at the maximum NANF output power (green) for each respective linewidth configuration. Inset shows the intensity plot versus $\Delta\lambda$ from -1 nm to 1 nm for different powers.

This $P_{th(SRS)}$ estimate is based on our experiments where SRS peaks were not present for output powers below 1400 kW. Neglecting propagation losses, from the SRS power threshold equation $P_{th(SRS)} = (16A_{eff})/(g_R L_{eff})$ [50], we can determine the Raman gain coefficient (g_R), using $A_{eff} = 254\ \mu m^2$ for our NANF and effective fiber length ($L_{eff} = 104.5$ m). This yields a $g_R \approx 2.7 \times 10^{-14}$ m/W. Employing the calculated g_R and solving for $P_{th(SRS)} = 2300$ W, we obtain a maximum NANF length of 63.6 m. This analysis ensures that the spectral features arising from the SRS response of atmospheric nitrogen are avoided in the NANF when delivering our narrow-linewidth laser.

Similarly, one can estimate the SBS response and determine the power threshold before encountering detrimental backscatter at the laser source. For clarity, we focus on the SBS effects arising from the delivery fiber isolated from the high-power source. We compare the expected SBS response of a solid-core delivery fiber with equivalent MFD = 17 μm to that of the NANF. The SBS power threshold can be obtained from $P_{th(SBS)} = (21A_{eff})/(g_{B(\Delta\nu)} L_{eff})$ [50], where $g_{B(\Delta\nu)}$ is the linewidth dependant Brillouin gain coefficient. In this example, we neglect fiber losses; the source linewidth is 38 GHz, $A_{eff} = 227\ \mu m^2$, and $L_{eff} = 104.5$ m. For the NANF, the estimate Brillouin gain coefficient contribution from nitrogen is $g_{B_{N_2}(\Delta\nu)} \approx 5.4 \times 10^{-15}$ m/W [51,52], and the Brillouin gain coefficient due to the optical field overlap with silica glass is $g_{B_{Si}(\Delta\nu)} \approx 3.3 \times 10^{-17}$ m/W. As a result, $g_{B(\Delta\nu)} = g_{B_{N_2}(\Delta\nu)} + g_{B_{Si}(\Delta\nu)} \approx 5.4 \times 10^{-15}$ m/W. Therefore, the corresponding SBS power threshold for a 104.5 m long NANF delivery fiber filled with atmospheric nitrogen is ~8.5 kW. Clearly, if the fiber is in vacuum, the gas contribution is negligible, resulting in a SBS threshold of ~1.4 MW. On the other hand, a comparable solid-core fiber would be limited to 170 W power delivery, due to its significantly higher SBS gain ($\approx 2.69 \times 10^{-13}$ m/W) for a 38 GHz signal. Subsequently, we calculate the maximum fiber length before reaching the SBS power threshold when transmitting our 38 GHz linewidth, 1.8 kW average power laser. Once more, without losses, this leads to maximum fiber lengths of 9.9 m for the solid-core fiber, 493 m for the atmospheric nitrogen-filled NANF, and 80.7 km when the NANF core is evacuated.

4. CONCLUSIONS

We have demonstrated 2.2 kW power delivery with 86 GHz linewidth at 1080 nm, through a 104.5 m long single-mode HCF. This was enabled by an in-house fabricated low-loss five-tube NANF, with a measured loss of 0.79 dB/km at 1080 nm. The transmission efficiency was 95% with near-diffraction-limited output beam quality. Similar performance was achieved for laser linewidths of 63 GHz and 38 GHz, resulting in output powers of 2.18 kW, and 1.7 kW, with transmission efficiencies of 94.5% and 95.3%, respectively. The NANF effectively mitigates nonlinear SRS and SBS effects from glass. However, at high powers, additional discrete frequency peaks appear in the output spectrum, due to rotational SRS from atmospheric nitrogen in the fiber's core. It is worth noting that these nonlinear distortions can be suppressed by filling the fiber core with a non-Raman active gas or by applying vacuum. However, of interest would be to further study this effect to develop high-power gas-filled NANF lasers with tailored and potentially tunable emission wavelenghths.

Our results could pave the way for high-brightness narrow-linewidth fiber delivery systems for a broad range of applications. By preserving both the spatial and spectral attributes of the source at multi-kW power levels, these fibers can be deployed in the laser manufacturing process to improve volume throughput. NANFs can also be instrumental in power scaling narrow-linewidth fiber laser amplifiers, as the output power of such systems is often limited by SBS originating from the delivery fiber. Finally, NANFs could enable novel coherent and spectral beam combining architectures by providing an avenue to extend the distance from the laser sources to the output beam combiner, and to eliminate free-space optics typically required to transport multi-kW powers.

Funding. Army Research Office (W911NF1910426); U.S. Navy (N68335-20-C0862).

Acknowledgment. M.C. acknowledges support from SPIE, the Directed Energy Professional Society, and the Northrop Grumman graduate scholarship programs. The authors thank David Scerbak from Coherent Corp. for collaboration and access to the high-power testing facilities. This work was supported in part by the Army Research Office (W911NF1910426) and the Department of the Navy (N68335-20-395-C0862).

Disclosures. The authors declare no conflicts of interest.

Data availability. Data underlying the results presented in this paper are not publicly available at this time, but may be obtained from the authors upon reasonable request.

REFERENCES

1. Y. Zhao, J. Zhu, W. He, *et al.*, "3D printing of unsupported multi-scale and large-span ceramic via near-infrared assisted direct ink writing," Nat. Commun. **14**, 2381 (2023).
2. C. Gaida, M. Gebhardt, T. Heuermann, *et al.*, "Watt-scale super-octave mid-infrared intrapulse difference frequency generation," Light Sci. Appl. **7**, 94 (2018).
3. T. Balciunas, C. Fourcade-Dutin, G. Fan, *et al.*, "A strong-field driver in the single-cycle regime based on self-compression in a Kagome fibre," Nat. Commun. **6**, 6117 (2015).
4. F. Emaury, C. F. Dutin, C. J. Saraceno, *et al.*, "Beam delivery and pulse compression to sub-50 fs of a modelocked thin-disk laser in a gas-filled Kagome-type HC-PCF fiber," Opt. Express **21**, 4986–4994 (2013).
5. D. Cruz-Delgado, S. Yerolatsitis, N. K. Fontaine, *et al.*, "Synthesis of ultrafast wavepackets with tailored spatiotemporal properties," Nat. Photonics **16**, 686–691 (2022).
6. F. Poletti, N. V. Wheeler, M. N. Petrovich, *et al.*, "Towards high-capacity fibre-optic communications at the speed of light in vacuum," Nat. Photonics **7**, 279–284 (2013).
7. J. R. Hayes, S. R. Sandoghchi, T. D. Bradley, *et al.*, "Antiresonant hollow core fiber with an octave spanning bandwidth for short haul data communications," J. Lightwave Technol. **35**, 437–442 (2017).
8. G. T. Jasion, H. Sakr, J. R. Hayes, *et al.*, "0.174 dB/km hollow core double nested antiresonant nodeless fiber (DNANF)," in *Optical Fiber Communication Conference (OFC)* (Optica Publishing Group, 2022), paper Th4C.7.
9. J. H. Osório, F. Amrani, F. Delahaye, *et al.*, "Hollow-core fibers with reduced surface roughness and ultralow loss in the short-wavelength range," Nat. Commun. **14**, 1146 (2023).
10. D. J. Richardson, J. Nilsson, and W. A. Clarkson, "High power fiber lasers: current status and future perspectives [invited]," J. Opt. Soc. Am. B **27**, B63–B92 (2010).
11. S. Du, T. Qi, D. Li, *et al.*, "10 kW fiber amplifier seeded by random fiber laser with suppression of spectral broadening and SRS," IEEE Photon. Technol. Lett. **34**, 721–724 (2022).
12. J. H. Osório, J. B. Rosolem, F. R. Bassan, *et al.*, "Hollow-core photonic crystal fibers for power-over-fiber systems," Opt. Fiber Technol. **73**, 103041 (2022).
13. J. W. Dawson, M. J. Messerly, R. J. Beach, *et al.*, "Analysis of the scalability of diffraction-limited fiber lasers and amplifiers to high average power," Opt. Express **16**, 13240–13266 (2008).
14. C. Jauregui, J. Limpert, and A. Tünnermann, "High-power fibre lasers," Nat. Photonics **7**, 861–867 (2013).
15. V. R. Supradeepa, "Stimulated brillouin scattering thresholds in optical fibers for lasers linewidth broadened with noise," Opt. Express **21**, 4677–4687 (2013).
16. M. N. Zervas and C. A. Codemard, "High power fiber lasers: a review," IEEE J. Sel. Top. Quantum Electron. **20**, 219–241 (2014).
17. K. Shima, S. Ikoma, K. Uchiyama, *et al.*, "5-kW single stage all-fiber Yb-doped single-mode fiber laser for materials processing," Proc. SPIE **10512**, 105120C (2018).
18. J.-P. Negel, A. Austerschulte, M. M. Vogel, *et al.*, "Delivery of 800 W of nearly diffraction-limited laser power through a 100 m long multi-mode fiber," Laser Phys. Lett. **11**, 055104 (2014).
19. C. Röhrer, C. A. Codemard, G. Kleem, *et al.*, "Preserving nearly diffraction-limited beam quality over several hundred meters of transmission through highly multimode fibers," J. Lightwave Technol. **37**, 4260–4267 (2019).
20. T. Matsui, K. Tsujikawa, T. Okuda, *et al.*, "Effective area enlarged photonic crystal fiber with quasi-uniform air-hole structure for high power transmission," IEICE Trans. Commun. **E103.B**, 415–421 (2020).
21. T. Okuda, Y. Fujiya, S. Goya, *et al.*, "Beam transmission technology by photonic crystal fiber to realizes high-precision and high-efficiency laser processing technology," Mitsubishi Heavy Ind. Tech. Rev. **57**, 1–5 (2020).
22. R. F. Cregan, B. J. Mangan, J. C. Knight, *et al.*, "Single-mode photonic band gap guidance of light in air," Science **285**, 1537–1539 (1999).
23. R. Amezcua-Correa, N. G. R. Broderick, M. N. Petrovich, *et al.*, "Optimizing the usable bandwidth and loss through core design in realistic hollow-core photonic bandgap fibers," Opt. Express **14**, 7974–7985 (2006).
24. R. Amezcua-Correa, F. Gérôme, S. G. Leon-Saval, *et al.*, "Control of surface modes in low loss hollow-core photonic bandgap fibers," Opt. Express **16**, 1142–1149 (2008).
25. W. Belardi and J. C. Knight, "Effect of core boundary curvature on the confinement losses of hollow antiresonant fibers," Opt. Express **21**, 21912–21917 (2013).
26. W. Shere, E. N. Fokoua, G. T. Jasion, *et al.*, "Designing multi-mode antiresonant hollow-core fibers for industrial laser power delivery," Opt. Express **30**, 40425–40440 (2022).
27. V. Michaud-Belleau, E. N. Fokoua, T. D. Bradley, *et al.*, "Backscattering in antiresonant hollow-core fibers: over 40 dB lower than in standard optical fibers," Optica **8**, 216–219 (2021).
28. M. S. Habib, C. Markos, and R. Amezcua-Correa, "Impact of cladding elements on the loss performance of hollow-core anti-resonant fibers," Opt. Express **29**, 3359–3374 (2021).
29. S.-F. Gao, Y.-Y. Wang, W. Ding, *et al.*, "Hollow-core conjoined-tube negative-curvature fibre with ultralow loss," Nat. Commun. **9**, 2828 (2018).
30. F. Amrani, J. H. Osório, F. Delahaye, *et al.*, "Low-loss single-mode hybrid-lattice hollow-core photonic-crystal fibre," Light Sci. Appl. **10**, 7 (2021).
31. B. Debord, A. Amsanpally, M. Chafer, *et al.*, "Ultralow transmission loss in inhibited-coupling guiding hollow fibers," Optica **4**, 209–217 (2017).
32. F. Poletti, "Nested antiresonant nodeless hollow core fiber," Opt. Express **22**, 23807–23828 (2014).
33. H. Sakr, Y. Chen, G. T. Jasion, *et al.*, "Hollow core optical fibres with comparable attenuation to silica fibres between 600 and 1100 nm," Nat. Commun. **11**, 6030 (2020).
34. H. C. Mulvad, S. A. Mousavi, V. Zuba, *et al.*, "Kilowatt-average-power single-mode laser light transmission over kilometre-scale hollow-core fibre," Nat. Photonics **16**, 448–453 (2022).
35. A. D. Pryamikov, A. S. Biriukov, A. F. Kosolapov, *et al.*, "Demonstration of a waveguide regime for a silica hollow-core microstructured optical fiber with a negative curvature of the core boundary in the spectral region >3.5 μm," Opt. Express **19**, 1441–1448 (2011).
36. E. N. Fokoua, S. A. Mousavi, G. T. Jasion, *et al.*, "Loss in hollow-core optical fibers: mechanisms, scaling rules, and limits," Adv. Opt. Photon. **15**, 1–85 (2023).
37. D. C. Jones, C. R. Bennett, M. A. Smith, *et al.*, "High-power beam transport through a hollow-core photonic bandgap fiber," Opt. Lett. **39**, 3122–3125 (2014).
38. S. Hädrich, J. Rothhardt, S. Demmler, *et al.*, "Scalability of components for kw-level average power few-cycle lasers," Appl. Opt. **55**, 1636–1640 (2016).
39. G. Palma-Vega, F. Beier, F. Stutzki, *et al.*, "High average power transmission through hollow-core fibers," in *Laser Congress (ASSL)* (Optica Publishing Group, 2018), paper ATh1A.7.
40. X. Zhu, D. Wu, Y. Wang, *et al.*, "Delivery of cw laser power up to 300 watts at 1080 nm by an uncooled low-loss anti-resonant hollow-core fiber," Opt. Express **29**, 1492–1501 (2021).
41. M. Cooper, J. Wahlen, S. Wittek, *et al.*, "600 W single mode CW beam delivery via anti-resonant hollow core fiber," J. Directed Energy **7** (2022).
42. X. Zhu, F. Yu, D. Wu, *et al.*, "Laser-induced damage of an anti-resonant hollow-core fiber for high-power laser delivery at 1 μm," Opt. Lett. **47**, 3548–3551 (2022).
43. M. S. Habib, J. E. Antonio-Lopez, C. Markos, *et al.*, "Single-mode, low loss hollow-core anti-resonant fiber designs," Opt. Express **27**, 3824–3836 (2019).
44. A. E. Siegman, "How to (maybe) measure laser beam quality," in *DPSS (Diode Pumped Solid State) Lasers: Applications and Issues* (Optica Publishing Group, 1998), paper MQ1.
45. A. Flores, C. Robin, A. Lanari, *et al.*, "Pseudo-random binary sequence phase modulation for narrow linewidth, kilowatt, monolithic fiber amplifiers," Opt. Express **22**, 17735–17744 (2014).
46. A. Kliner, K.-C. Hou, M. Plötner, *et al.*, "Fabrication and evaluation of a 500 W cladding-light stripper," Proc. SPIE **8616**, 86160N (2013).
47. S. A. Mousavi, H. C. H. Mulvad, N. V. Wheeler, *et al.*, "Nonlinear dynamic of picosecond pulse propagation in atmospheric air-filled hollow core fibers," Opt. Express **26**, 8866–8882 (2018).

48. A. M. Zheltikov, "An analytical model of the rotational Raman response function of molecular gases," J. Raman Spectrosc. **39**, 756–765 (2008).
49. C. Meißner, J. I. Hölzer, and T. Seeger, "Determination of N_2–N_2 and N_2–O_2 S-branch Raman linewidths using time-resolved picosecond pure rotational coherent anti-Stokes Raman scattering," Appl. Opt. **58**, C47–C54 (2019).
50. G. P. Agrawal, *Nonlinear Fiber Optics* (Academic, 2019).
51. F. Yang, F. Gyger, and L. Thévenaz, "Intense Brillouin amplification in gas using hollow-core waveguides," Nat. Photonics **14**, 700–708 (2020).
52. M. Galal, L. Zhang, S. Gao, *et al.*, "Study of backward Brillouin scattering in gas-filled anti-resonant fibers," APL Photon. **8**, 086104 (2023).